INORGANIC CHEMISTRY FRONTIERS

RESEARCH ARTICLE

View Article Online
View Journal | View Issue

Cite this: *Inorg. Chem. Front.*, 2022, **9**, 2087

Crystal–amorphous NiO/MoO_2 with a high-density interface for hydrogen evolution†

Ya-Nan Zhou,[a] Meng-Xuan Li,[a] Zhuo-Ning Shi,[a] Jian-Cheng Zhou,[a] Bin Dong, *[a] Wenchun Jiang,[b] Bin Liu,[a] Jian-Feng Yu[a] and Yong-Ming Chai*[a]

Received 16th January 2022,
Accepted 25th February 2022

DOI: 10.1039/d2qi00136e

rsc.li/frontiers-inorganic

Developing high-density and uniform crystal–amorphous interfaces is highly desirable for the hydrogen evolution reaction (HER). Herein, crystal–amorphous NiO/MoO_2 with a coupled high-density interface has been designed to tailor the charge distribution to lower the reaction energy barrier for the HER. The obtained self-supported NiO/MoO_2-100-2, which is fabricated through a simple and versatile anodizing-assisted molten salt with a MoNi substrate, possesses high-density and a well-dispersed NiO crystal /amorphous MoO_2 heterojunction, benefiting local electron rearrangement and charge transfer. The NiO crystals are beneficial for the alkaline water dissociation to rapidly generate active hydrogen (Volmer step), therefore facilitating the subsequent Heyrovsky and Tafel steps to occur in the amorphous MoO_2 region. NiO/MoO_2-100-2 exhibits superior HER activity with a low overpotential of 48 mV at 10 mA cm^{-2}, a small Tafel slope of 51.5 mV dec^{-1} and robust stability, which can be chalked up to the more available actives sites, enhanced conductivity and favorable H adsorption sites derived from the modulated charge and d-band structure near the Fermi level.

1. Introduction

Electrochemical water splitting is an environmentally friendly route to the generation of hydrogen that has aroused extensive interest due to its great potential to replace dirty fossil fuels.[1–3] The hydrogen evolution reaction (HER), as the cathode reaction in water electrolysis, suffers from high energy consumption and serious resource wastage, especially under alkaline conditions.[4–6] To tackle this problem pointedly, the development of high-efficiency electrocatalysts is the top priority at present. However, the benchmark Pt-based catalysts are limited by low reserves and high costs. As a result, Earth-abundant non-noble metal materials are predicted as holy grails for future sustainable hydrogen production.

Transition metal oxides are generally regarded as HER inactive materials due to unsuitable hydrogen adsorption energy and inert electron transport.[7–9] Particularly for nickel oxide (NiO), which is an ideal catalyst for water adsorption and dissociation in an alkaline medium, the calculated ΔG_{H^*} value is −0.27 eV or −0.55 eV,[10,11] which is too negative to easily desorb active hydrogen, while according to the Sabatier principle, better catalytic performance is based on moderate bonding to the active species.[12,13] Therefore, combining NiO with materials with better hydrogen desorption capability to generate efficient catalytic sites for fast hydrogen adsorption/desorption is necessary. Encouragingly, molybdenum dioxide (MoO_2) featuring a metallic character possesses a ΔG_{H^*} value of around 0.15 eV, exhibiting outstanding potential as a hydrogen adsorption promoter, thanks to the lower unoccupied orbital in the alkaline electrolytes.[14–16] Herein, the coupling of NiO and MoO_2 is a promising strategy for better HER efficiency. However, the inherently poor conductivity and activity of NiO and MoO_2 remain the primary challenge. Intrinsically, its motivation lies in local electron configuration arrangement to optimize the electron transport capacity together with adsorption/dissociation of H_2O and hydrogen, which are intertwined with the formed lattice, charges, and spin ordering in obtained catalysts. For the HER, the electron distribution and band structure around the Fermi energy level are extremely remarkable characteristics.[17–19] In this regard, the tailoring for spin ordering and orbital filling of metal ions is perceived as a brand new and efficient approach. Taking all these into account, generating a new strong coupling crystal interface with a unique atomic and electronic structure is expected to bridge the gap between NiO, MoO_2 and favorable catalytic activity.

Preferentially, the development of a unique crystal–amorphous NiO/MoO_2 interface with high density and good distri-

[a]*State Key Laboratory of Heavy Oil Processing, College of Chemistry and Chemical Engineering, China University of Petroleum (East China), Qingdao 266580, PR China. E-mail: dongbin@upc.edu.cn, ymchai@upc.edu.cn; Fax: +86-532-86981156; Tel: +86-532-86981156*

[b]*College of New Energy, China University of Petroleum (East China), Qingdao, 266580, PR China*

† Electronic supplementary information (ESI) available. See DOI: https://doi.org/10.1039/d2qi00136e

bution is more attractive while challenging because the extraneous Ni and Mo source cannot be easily mixed uniformly. To solve this problem, the MoNi foam can be applied as the substrate to provide a well-mixed Mo and Ni source, thus the density and distribution of the interface may be ensured, whereas high-strength substrates characterized by the dense internal atomic arrangement or/and a glazed surface, including Mo, W, Ta, and their respective alloys, cannot be treated easily by conventional methods, such as solvothermal reaction and electro-deposition.[20] Prospectively, molten salt synthesis has emerged as a facile and environmentally friendly method. For example, Li *et al.* reported a molten salt $NaNO_3$ system, with which ultra-thin RuO_2 nanosheets are prepared successfully for water oxidation.[21] Wang's team also employed the molten salt method to disperse Ni ions on TiO_2.[22] Unlike ordinary solvents, the high solubility, space confinement effect, and strong polarization provided by this special ionic liquid will inevitably have a profound impact on the morphology and electrochemical properties of compounds.[23] Given these, the molten salt is necessitated to activate MoNi substrates to obtain highly active and stable catalysts; in the present work, it is referred to as NiO/MoO_2.

Parallel to the desirable active interface, the generation of abundant defects, even amorphous phases by coupling NiO and MoO_2 is equally intriguing because of a larger proportion of unsaturated metal sites and randomly oriented bonds. Concretely, the structure adaptability of amorphous phases in the short-range can expedite the charge transfer between active sites and intermediates as well as contribute to spin-state manipulation, which is supposed to synergistically increase hydrogen evolution with the NiO/MoO_2 interface.[24,25] The mutual coupling of strategies enables the simultaneous optimization of multiple constraints to boost hydrogen evolution.

Inspired by all the above discussion, a self-supported crystal–amorphous NiO/MoO_2 heterointerface directly derived from MoNi foam with a high-density interface has been prepared *via* a versatile molten-salt method assisted by anodizing. Scheme 1 schematically shows the synthesis process. The pre-anodizing of MoNi foam produces partly oxidized and stripped NiO/MoO_2 species and disturbed surface structure (NiO/MoO_2-100), which is conducive to subsequent molten salt treatment and morphological transformation. After being etched by molten salt, NiO/MoO_2-100 becomes metastable and meanwhile forms a high-density NiO crystal/amorphous MoO_2 interface on the brand new stripped layered structure, which is proved to facilitate electron transfer and intermediate adsorption/desorption with a low overpotential of 48 mV at 10 mA cm^{-2} and a small Tafel slope of 51.5 mV dec^{-1}. DFT calculation also confirms the regulated charge arrangement near the Fermi energy, which is accompanied by the magnetic moment change. More importantly, the long-term durability further verifies the practicability of the molten-salt method, which provides new possibilities for high-performance catalyst design.

2. Experimental section

2.1. Chemicals

MoNi foam (thickness of 3 mm) was purchased from Kunshan Tengerhui Electronic Technology Co. Ltd. Ethanol (C_2H_5OH, AR), acetone (CH_3COCH_3, AR), dipotassium phosphate (K_2HPO_4), monopotassium phosphate (KH_2PO_4) and sodium chloride (NaCl) were purchased from Sinopharm Chemical Reagent Co. Ltd (Shanghai, China).

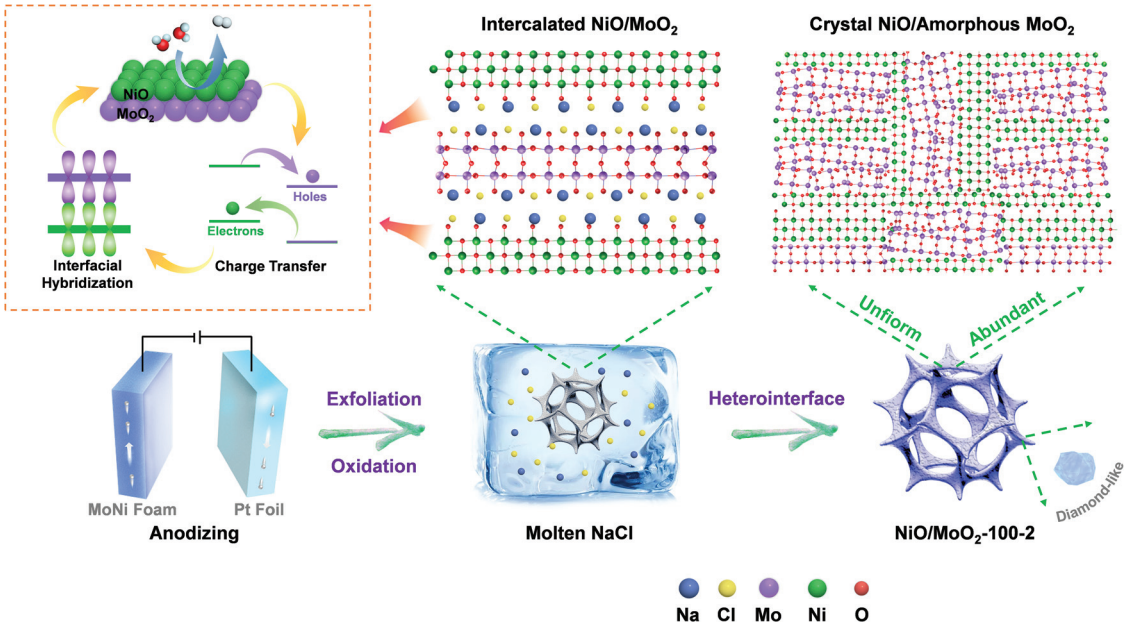

Scheme 1 Illustration of the fabrication process of the NiO/MoO_2-100-2 sample.

2.2. Preparation of NiO/MoO_2-*s*

NiO/MoO_2-*s* was obtained by anodic oxidation of MoNi foam. The purchased MoNi foam was directly washed with hydrochloric acid, acetone, ethanol and deionized water for 30 min, respectively, and then vacuum dried for later use. Then the cut MoNi foam (1 × 2 cm) was oxidized by a three-electrode system at 0.5 V in phosphate buffer with a Pt plate as the counter electrode and a saturated calomel electrode as the reference electrode. The oxidized MoNi foam is denoted as NiO/MoO_2-*s* (*s* indicates the anodic treatment time, seconds).

2.3. Preparation of NiO/MoO_2-*s*-*h* and Ni/Mo-*h*

The molten-salt method was proposed to produce the final NiO/MoO_2-*s*-*h*. The above NiO/MoO_2-*s* samples were immersed in molten NaCl at 800 °C for a certain time to acquire NiO/MoO_2-*s*-*h* (*h* indicates the treatment time, hours).

For comparison, Ni/Mo-*h* was synthesized by the same method as NiO/MoO_2-*s*-*h* using MoNi foam without anodizing.

2.4. Preparation of NiO and MoO_2

For comparison, NiO was synthesized by a similar procedure to NiO/MoO_2-100-2 except for using nickel foam as the support. MoO_2 was obtained by the same method as NiO/MoO_2-100 with molybdenum foil as the substrate.

3. Results and discussion

The final NiO/MoO_2-100-2 sample with a NiO crystal/amorphous MoO_2 heterostructure was fabricated by atypical two-step anodizing and molten-salt method process. The morphology transformation during this procedure is characterized by scanning electron microscopy (SEM) and transmission electron microscopy (TEM). For simplicity, NiO/MoO_2-100-2 was screened as a representative sample for correlated analysis. As shown in Fig. S1a and b,† the commercial MoNi foam with a porous network structure possesses plenty of accumulated spherical clusters on the skeleton about 2.5 μm in diameter, and Mo and Ni are well mixed and distributed, benefiting the formation of high-density and homogeneous NiO/MoO_2 interfaces. After anodic oxidation, the obtained NiO/MoO_2-100 shows a relatively smooth surface where the nanoislands become fuzzy and tend to be flat (Fig. 1 and Fig. S1c and d†).

These activated surfaces with perturbed atomic arrangements are conducive to subsequent molten-salt method treatment. As expected, with two hours of immersion in molten NaCl (NiO/MoO_2-100-2), the closely packed irregular diamond-like nanoparticles were easily detected, most of which are 600 nm in diameter (Fig. 1 and Fig. S2†). The significantly smaller nanoparticles undoubtedly contribute to the increase in the specific surface area, therefore creating enough active sites to promote hydrogen production. The crucial role of anodizing is further corroborated by Ni/Mo-2 samples (Fig. S3†), whose average larger-diameter (1200 nm) nanoparticles are merely the products of further growth of original clusters on pure MoNi foam with slight integration, unlike NiO/MoO_2-100-2, which is the product of the relatively thorough post-integration growth. X-ray diffraction (XRD) is performed to identify the samples' surface composition. Fig. S4a† first confirms that the main phase of MoNi foam is metallic Ni (JCPDS: 70-0989), while peaks of Mo species cannot be clearly discerned due to the shielding effect of the stronger peaks of Ni. For the result-

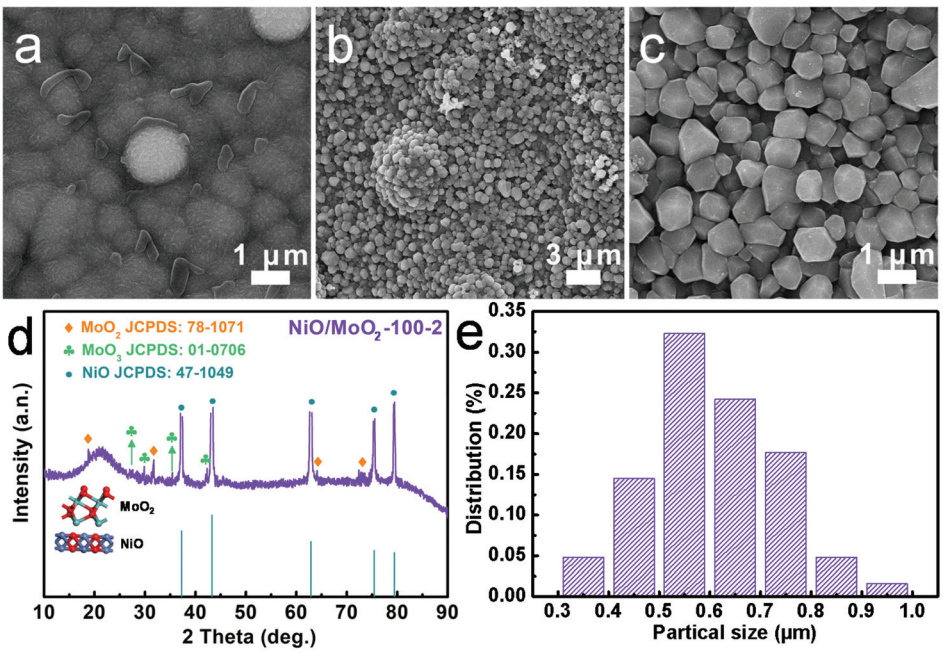

Fig. 1 Structure characterization of NiO/MoO_2-100 and NiO/MoO_2-100-2. SEM images of (a) NiO/MoO_2-100 and (b and c) NiO/MoO_2-100-2. (d) XRD pattern and (e) particle distribution of NiO/MoO_2-100-2.

ing NiO/MoO_2-100-2 (Fig. 1d), strong peaks at 37.1°, 43.2°, 62.9°, 75.4° and 79.4° match well with the (111), (200), (220), (311) and (222) crystal planes of NiO (JCPDS: 47-1049); and the signals of the (100), (−102), (122) and (−411) planes of MoO_2 (JCPDS: 78-1071) can also be roughly detected at 18.4°, 31.6°, 63.8° and 73.0°. In addition, the MoO_3 species can also be indexed at 27.4°, 29.6°, 35.6° and 42.4° (JCPDS: 01-0706) due to surface oxidation. These results suggest the coexistence of NiO and MoO_x components. In addition, the broad peak may result from finely dispersed nano-sized particles or low crystallinity. Compared with NiO/MoO_2-100 (Fig. S4b†), whose XRD peaks also show the presence of NiO, the diffraction pattern of NiO/MoO_2-100-2 becomes diffuse and wider, which demonstrates more defects after molten salt treatment.

Interestingly, the TEM image of NiO/MoO_2-100-2 stripped from the substrate shown in Fig. 2a and b clearly manifests the two-dimensional (2D) morphology, implying a previously well-verified phenomenon that during the reaction, molten NaCl can be inserted into NiO/MoO_2 to form a 2D layered material.[23,26] High-resolution TEM (Fig. 2c and d) confirms the presence of abundant NiO crystal/amorphous MoO_2 heterointerfaces thanks to well mixed Mo and Ni in MoNi foam, where two lattice fringe spacings can be observed, belonging to the *d*-spacing of 0.209 nm for the (200) crystal plane of NiO and 0.284 nm of the (−102) plane for monoclinic MoO_2, respectively, consistent with XRD analysis. In detail, Fig. S5† clearly shows the NiO/MoO_2 interface, where the detected 0.209 and 0.241 nm belong to NiO while the ambiguous crystals with the distance of 0.218 and 0.147 nm come from MoO_2.

The formation of the distinct crystals/amorphous in this work is mainly because of the unique MoNi foam, which is manufactured by deposition with a polymeric sponge as the substrate to form the Ni film–Ni coating–NiMo alloy structure. The Mo and Ni atoms in sandwich-like structures suffer from different moving rates to lead to the dense distribution of the heterophase. According to the earlier report, NiO can facilitate the dissociation of water in an alkaline electrolyte to generate active hydrogen, while amorphous areas are the active centers for hydrogen adsorption and desorption, thus synergistically boosting the HER process.[10,11,27] It is worth mentioning that the lattice plane of MoO_3 cannot be well observed due to the multi-defect structure. Note that the low valence-state Mo species are deemed to be active for the HER, and can serve as catalytic sites for hydrogen adsorption.[14–16] Furthermore, SEM mapping (Fig. 2e) shows that Ni, Mo, and O are uniformly distributed in the selected field. Energy-dispersive X-ray spectroscopy (EDX) results in Fig. S6† show the elementary composition and contents. Notably, it shows a much lower Mo (2.64 At.%) content than Ni content (68.43 At.%), which may result from the different dynamic migration rates of Ni and Mo from the interior of the MoNi foam substrate to the surface in the molten salt system, which can be laterally confirmed by the higher compactness of the pure molybdenum plate than that of nickel foam. Next, the possible growth mechanism of the nanosheet structure is discussed and proposed as follows.

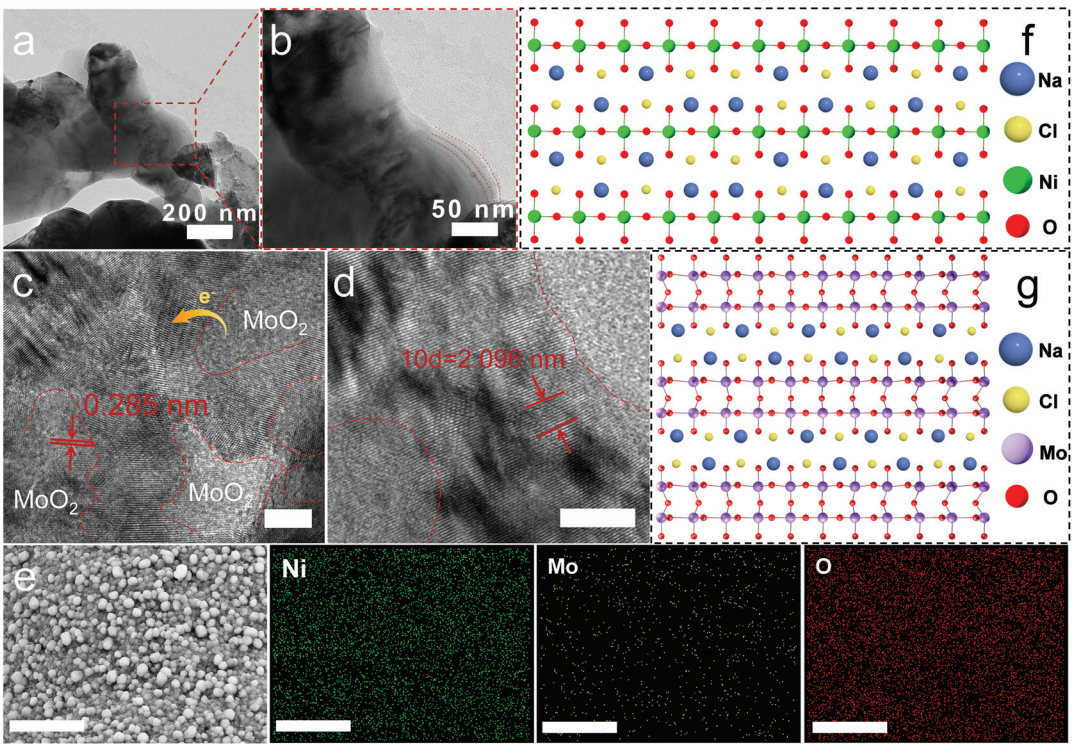

Fig. 2 Structural analysis of NiO/MoO_2-100-2. (a and b) TEM images. (c and d) HRTEM images, c, scale bar: 2 nm; d, scale bar, 3 nm. The red lines denote the crystal/amorphous interfaces. (e) SEM mapping, scale bar: 10 μm. Atomic structures of (f) NiO and (g) MoO_2.

First, according to the Arrhenius equation,[28] the mathematical relationship of k_a and k_b that represents the reaction rate constant of supposed growth direction [001] and [100], respectively, is first expressed as below:

$$\frac{k_b}{k_a} = e^{\frac{E_a - E_b}{RT}}$$

where E_a and E_b are the activation energy in the different growth directions, R is the molar gas constant, and T is the reaction temperature. Based on previous research, molten salt ions are inclined to intercalate into the interlayer space rather than into the crystal lattice, which is analogous to the exfoliation of 2H-MoS_2 by Li^+,[29,30] thus lowering the activation energy (E_b) of the [110] direction. As a result, the value of the k_b over k_a increases, leading to a lamellar structure. Theoretically, the two-step process of the generation of 2D morphology can be summarized.[31,32] The first step is the nucleation of $[MoO_6]_{octahedron}$ and $[NiO_6]_{octahedron}$ seeds and the second step is the growth of the crystal on the basis of the assembly of these seeds driven by molten salt ions (Fig. 2f and g). It is remarkable that NaCl can be readily extracted from deionized water for recycling, which makes this method environmentally benign and cost-effective for large-scale industrialization.

Further, X-ray photoelectron spectroscopy (XPS) is employed to investigate the surface composition of NiO/MoO_2-100-2. The full scan spectrum confirms the presence of Ni, Mo, and O elements again (Fig. S7a†). The deconvoluted Ni 2p region contains two pairs of typical peaks accompanied by the satellite peaks (labeled as Sat.) (Fig. 3a), which can be reliably assigned to the NiO ($2p_{3/2}$ at 856.1 eV and $2p_{1/2}$ at 873.4 eV) and Ni^0 ($2p_{3/2}$ at 854.1 eV and $2p_{1/2}$ at 871.6 eV) from the substrate.[33–36] In the Mo 3d spectrum (Fig. 3b), the coexistence of Mo^{3+}, Mo^{4+} and Mo^{6+} is substantiated by peaks at 231.9 eV, 232.3 eV and 235.6 eV, respectively.[37,38] Moreover, the perturbed electronic structure on the surface of NiO/MoO_2-100-2 *via* the molten-salt method can be discerned by the slight negative shift of Ni 2p (Fig. S7b†) and positive shift of Mo 3d peaks compared with the NiO/MoO_2-100 precursor. The O 1s spectrum can be fitted into lattice oxygen (O1 at 529.7 eV), oxygen defects (O2 at 530.2 eV), and surface-adsorbed oxygen species (O3 at 531.7 eV), respectively (Fig. S7c†).[39,40] The concentration of oxygen defects in the final catalyst increases to 35.6% from 31.4% of the precursor. The accumulated oxygen vacancies are conducive to electron rearrangement by acting as electron capture sites to regulate the coordination environments and electronic states of surface adsorbents. Meanwhile, the oxygen vacancies can activate their adjacent oxygen atoms toward hydrogen adsorption and facilitate water dissociation, in turn substantially improving the HER performance.[41] These XPS results suggest the local rearranged electronic structure of NiO/MoO_2-100-2 after the molten-salt method treatment.

The HER performance of all the prepared samples was also measured through three-electrode configuration in 1 M KOH. Fig. 4a shows the related polarization curves, and the target NiO/MoO_2-100-2 exhibits the best HER activity with a required overpotential of 48 mV at 10 mA cm^{-2}, superior to NiO/MoO_2-100 (204 mV), Ni/Mo-2 (198 mV) and other reported NiO-based catalysts. Intriguingly, when the current density is above 18 mA cm^{-2}, its activity is even better than that of the commercial Pt/C benchmark catalyst. The superiority of the NiO/MoO_2 heterostructure is also highlighted by the lower HER activity of single NiO and MoO_2 in Fig. S8.† Expectedly, the ratio of MoO_2 to NiO has a significant impact on the HER activity, which is determined by the anodizing and molten-salt process. Thus, the influence of these two variables on the ratio of MoO_2 and NiO and catalytic performance has been further investigated. In comparison, various anodizing times (50 s, 100 s, 150 s, and 200 s) are researched to clarify the role of pre-oxidation. As shown in Fig. S9a,† the HER performance of control samples increases first and then decreases rapidly with increasing anodic oxidation time, and the optimal time is 100 s, which can be reasonably attributed to the inadequate/excessive activation that leaves the induced NiO/MoO_2 inappropriate (too much MoO_2) for hydrogen evolution. Similarly, this reason can be applied to the phenomenon after changing the molten-salt method time, which results in excessive production of NiO (Fig. S9b†). Based on these, we speculate that the induced electron redistribution of the NiO/MoO_2 heterointerface in the molten salt system is also accountable for the different HER performance. Besides, the water oxidation

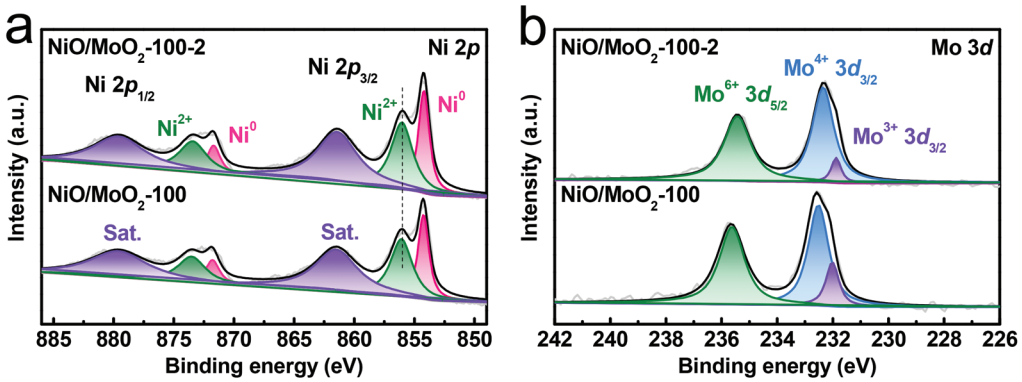

Fig. 3 XPS of (a) Ni 2p and (b) Mo 3d of NiO/MoO_2-100 and NiO/MoO_2-100-2.

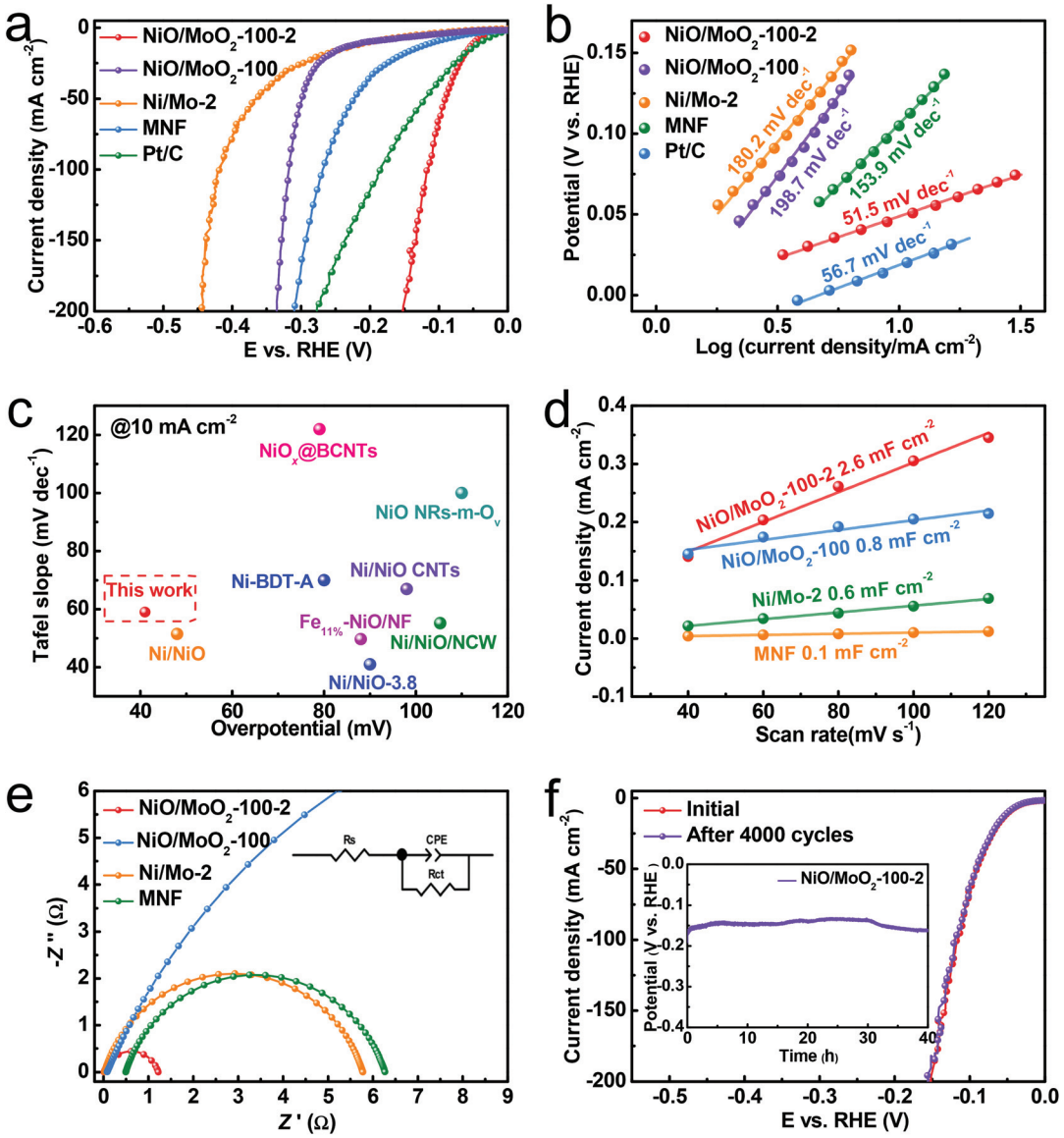

Fig. 4 Electrochemical measurements of the obtained NiO/MoO_2-100-2 sample in 1 M KOH. (a) Polarization curves and (b) the corresponding Tafel plots. (c) Comparison of the overpotential at 10 mA cm^{-2} and Tafel slope between NiO/MoO_2-100-2 and the reported NiO-based catalysts (Table S1†). (d) C_{dl} value. (e) Nyquist plots fitted to the model inset. (f) Polarization curves of NiO/MoO_2-100-2 before and after 4000 CV scans. The inset is the chronopotential curve at 100 mA cm^{-2}.

activity of the best-performing NiO/MoO_2-100-2 is also acceptable (Fig. S10†). The corresponding Tafel slopes calculated from polarization curves are depicted in Fig. 4b to grant access to the HER kinetic process.[42] The much smaller Tafel slope of 51.5 mV dec^{-1} for NiO/MoO_2-100-2 than NiO/MoO_2-100 (198.7 mV dec^{-1}), Ni/Mo-2 (180.2 mV dec^{-1}), Pt/C (56.7 mV dec^{-1}) and other control materials indicates that the rate-determining step changes from the Volmer step to Volmer–Heyrovsky step.[43] The influence of time of the molten-salt method and anodizing time exerted on the electron structure can be perceived by a series of Tafel plots (Fig. S11†). Furthermore, double-layer capacitance (C_{dl}) is evaluated by a range of cyclic voltammetry (CV) curves at 0.21 V *vs.* RHE (Fig. S12†) to assess the electrochemical active surface area. As expected, NiO/MoO_2-100-2 has the highest C_{dl} value (Fig. 4d), indicating that the increased active sites play a significant role in activity enhancement. In order to set forth the contribution of the surface area and intrinsic activity of samples to the HER, we also normalized polarization curves by the electrochemical active surface area, as shown in Fig. S13.†NiO/MoO_2-100-2 still shows admirable HER activity compared to the control sample NiO/MoO_2-100 and Ni/Mo-2, indicating that the inherent activity of NiO/MoO_2-100-2 improves due to the more intimate interactions between Ni and Mo caused by molten-salt treatment.

As a prevailing criterion for charge-transfer kinetics of the electrocatalytic process, electrochemical impedance spectroscopy (EIS) data are fitted *via* the inset circuit model shown in Fig. 4e and Fig. S14.† Obviously, as reflected from the semi-

circle diameter, the charge-transfer resistances of NiO/MoO_2-100-2 are much lower than that of other samples, signifying the favorable charge transfer capability. In order to obtain an insight into the stability of NiO/MoO_2-100-2 in the alkaline HER, the polarization curves before and after 4000 CV cycles are first collected in Fig. 4f and no distinct difference can be observed. Moreover, electrocatalytic HER is allowed to proceed for 40 h at a current density of 50 mA cm^{-2} with negligible degradation (illustrated in Fig. 4f). Fig. S15† shows that the morphology after the stability test remains unchanged and the crystal plane of NiO is well preserved, which together suggests the admirable durability benefitting from the inherent strong adhesion of the NiO/MoO_2-100-2 catalyst using the substrate as the metal source. XRD also discerned the NiO and MoO_2 phases after the 40 h HER tests (Fig. S16†), while the wider XRD peaks may indicate that the catalyst surface also consists of a NiO/MoO_2 heterostructure with more defects. The Ni 2p XPS shifts to a lower bonding energy, meanwhile the Mo 3d XPS moves to higher bonding energy, and no new valence can be deconvoluted (Fig. S17a–c†). For the O 1s spectrum, the content of defective O further increases to 43.2%, implying the newly produced oxygen defects, which is in line with the XRD result. These characterization studies after HER measurement indicate that the surface of NiO/MoO_2-100-2 is partially consumed under such a negative potential and alkaline electrolyte, and the newly formed defective species can still serve as highly efficient active centers.

Furthermore, to gain a deeper insight into the significance of the integration of NiO and MoO_2, it is necessary to figure out the spin state. According to the crystal field theory, when the electrons rearrange, the splitting of energy levels would result in additional energy. The Mo atom owns the $4d^5$ orbital with a higher energy level and it is a priority to be in a low spin state. Based on this, the possible electronic structure of MoO_2 can be deduced as shown in Fig. 5a. The ligand field of

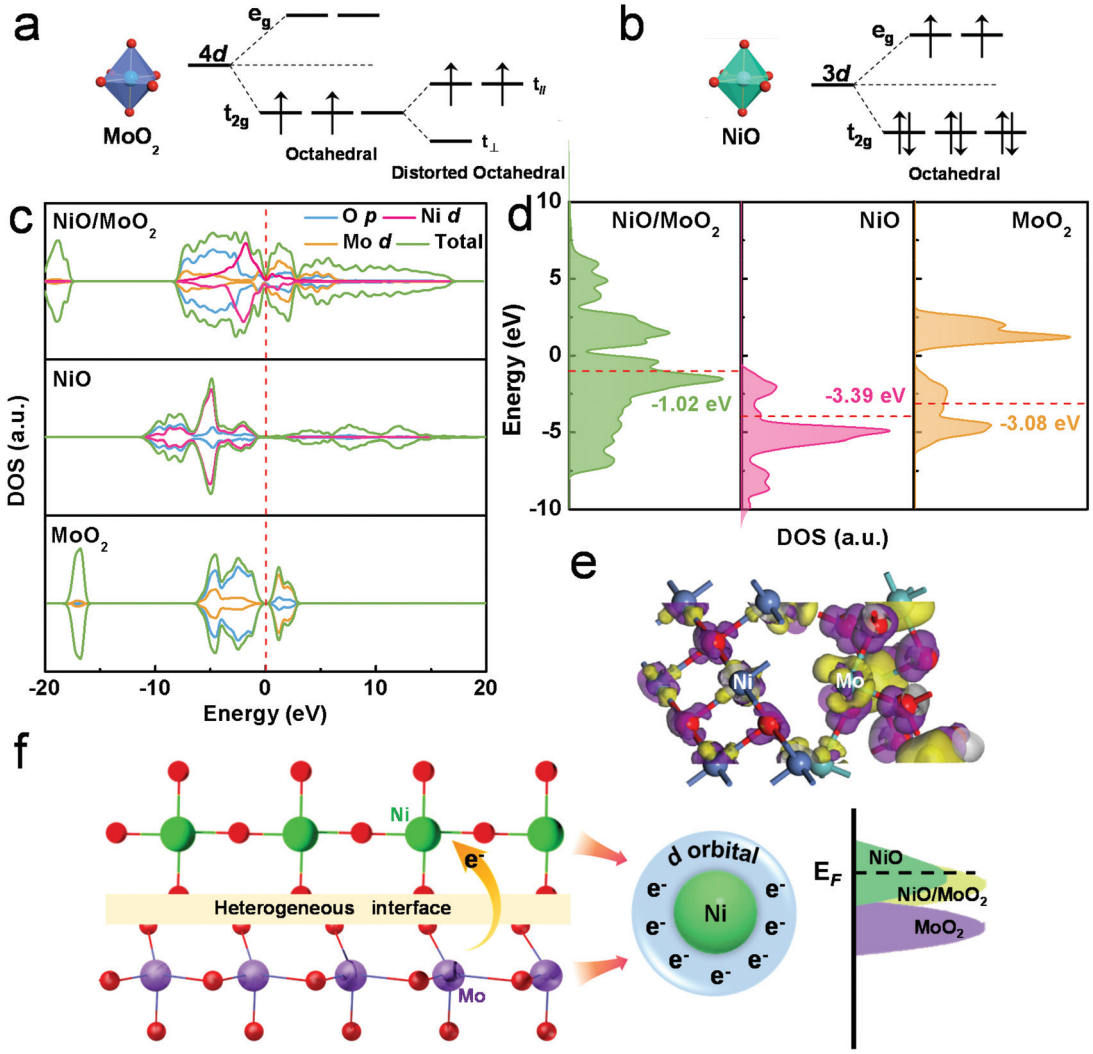

Fig. 5 (a) 4d orbital energy levels of Mo^{4+} and the Jahn–Teller effect, (b) schematic electronic configuration of the Ni cations in NiO, (c) DOS and PDOS and (d) d-band center level of NiO, MoO_2 and NiO/MoO_2, respectively, (e) electron density difference of the NiO/MoO_2 interface, (f) schematic illustration of the electron transfer of the Mo and Ni atom, and the valence band of NiO, MoO_2 and NiO/MoO_2.

Mo^{4+} can split the 4d orbital into t_{2g} and e_g sets, therefore the two electrons are prone to lie in the t_{2g} orbit. Due to the asymmetric occupation in degenerate orbitals, the two electrons occupy the $t_{\|}$ orbital, resulting in a lower energy level.[44] Similar splits can happen to Ni^{2+}, while the orbit structures of $t_{2g}^6e_g^2$, and e_g orbitals have been equally occupied, thus there is no further splitting (Fig. 5b).

In a nutshell, MoO_2 and NiO both possess lone pair electrons. Previous reports have indicated that the lone pair electrons of nanomaterials can induce strong interactions between them, thus improving reactivity and stability *via* partial or entire electron-donating.[45] In the present work, by means of a unique molten method, NiO can closely couple with MoO_2 on the interface of NiO/MoO_2, and the fluidity of unpaired electrons may lead to stronger electrical perturbations to enhance HER performance. Furthermore, the density of states (DOS) and partial DOS (PDOS) of the prepared catalysts were investigated within the density functional theory to verify the vital role of the NiO/MoO_2 heterostructure for hydrogen evolution. The possible structures of NiO, MoO_2 and NiO/MoO_2 have been constructed and optimized, as shown in Fig. S18.† The calculated DOS shown in Fig. 5c suggests the favorable conductivity of NiO/MoO_2 materials, and the d-electrons of Ni and Mo make the main contributions to the electron arrangement near the Fermi level. Besides, the level of the d-band center was also studied to quantify intuitively the electronic modulation.[46] As Fig. 5d shows, the d-band center energies of NiO and MoO_2 are −0.90 eV and −3.39 eV, respectively, which is too close or too far from the Fermi level, indicating that the metal–H bond is too strong or too weak to effectively desorb/trap hydrogen protons, thus resulting in low HER activity. Meanwhile, for the heterogeneous interface of NiO/MoO_2, the d-electrons of the two rearrange and the d-band center energy is −1.02 eV, falling somewhere in between and manifesting moderate hydrogen adsorption. The adjusted electrons of the NiO/MoO_2 interface are shown in Fig. 5e. The computed electron density difference shows the increased electron density (violet) of Ni atoms and decreased electron density (yellow) of Mo atoms, consistent with XPS results. Those results show that the electron distribution and energy band structures on the abundant interface of the NiO/MoO_2 heterostructure can be effectively regulated, as schematically illustrated in Fig. 5f, thus coordinating the adsorption and desorption capacity of the catalyst surface to H, therefore finally improving the HER electrocatalytic activity. Combined with all the above discussions, the final NiO/MoO_2-100-2 exhibits outstanding HER performance resulting from the optimized surface electron density and adsorption/desorption of intermediates as well as more available active sites.

4. Conclusions

In conclusion, a facile and practical anodizing-assisted molten-salt method has been proposed to construct a self-supported NiO/MoO_2 heterostructure with high-density crystal–amorphous interfaces directly using MoNi foam as the metal source. The synthesized diamond-like NiO/MoO_2-100-2 exhibits excellent HER performance in alkaline electrolytes, which can be ascribed to three main aspects: firstly, pre-anodizing ensures the activation of the inert surface of the substrate, thus facilitating the etching of subsequent molten salt to expose more active sites. Secondly, the formed high-density NiO crystal/amorphous MoO_2 heterostructure can induce changes in electron density and band structure near the Fermi level to further optimize adsorption and desorption properties as well as charge transfer capability. In detail, NiO works for alkaline water dissociation, promoting the Volmer step to produce active hydrogen, which guarantees the smooth implementation of the subsequent Heyrovsky and Tafel steps at the amorphous area. Thirdly, the regulated electron state of NiO and MoO_2 is also conductive to conductivity and adsorption capability optimization. This unique coupled crystal/amorphous structure, electron tailoring, and molten salt route are expected to provide new insights for advanced catalyst preparation.

Conflicts of interest

There are no conflicts to declare.

Acknowledgements

This work is financially supported by the National Natural Science Foundation of China (52174283) and the Shandong Provincial Natural Science Foundation (ZR2020MB044).

References

1 K. Yue, J. Liu, Y. Zhu, C. Xia, P. Wang, J. Zhang, Y. Kong, X. Wang, Y. Yan and B. Y. Xia, In situ ion-exchange preparation and topological transformation of trimetal-organic frameworks for efficient electrocatalytic water oxidation, *Energy Environ. Sci.*, 2021, **14**, 6546–6553.
2 S. Meng, S. Sun, Y. Qi, D. Jiang, W. Wei and M. Chen, Synthesis of an iron-doped 3D-ordered mesoporous cobalt phosphide material toward efficient electrocatalytic overall water splitting, *Inorg. Chem. Front.*, 2020, **7**, 3002–3010.
3 Y. Liu, Y. Yu, Z. Mu, Y. Wang, U. Ali, S. Jing and S. Xing, Urea-assisted enhanced electrocatalytic activity of MoS_2-Ni_3S_2 for overall water splitting, *Inorg. Chem. Front.*, 2020, **7**, 3588–3597.
4 X. X. Liu, K. L. Zhu, X. Zhang and P. Yang, MoS_2 nanosheets coupled with double-layered hollow carbon spheres towards superior electrochemical activity, *Electrochim. Acta*, 2022, **407**, 139929.
5 H. Yang, L. Gong, H. Wang, C. Dong, J. Wang, K. Qi, H. Liu, X. Guo and B. Y. Xia, Preparation of nickel-iron hydroxides by microorganism corrosion for efficient oxygen evolution, *Nat. Commun.*, 2020, **11**, 5075.

6 D. Li, Y. Xing, C. Zhou, Y. Lu, S. Xu, X. Shi, D. Jiang and W. Shi, Iron and nitrogen Co-doped $CoSe_2$ nanosheet arrays for robust electrocatalytic water oxidation, *Inorg. Chem. Front.*, 2021, **8**, 2725–2734.
7 X. Zhang, P. Yang and S. P. Jiang, Horizontally growth of WS_2/WO_3 heterostructures on crystalline g-C_3N_4 nanosheets towards enhanced photo/electrochemical performance, *J. Nanostruct. Chem.*, 2021, **11**, 367–380.
8 X. Zhang, P. Yang and S. P. Jiang, Ni clusters-derived 2D/2D layered $WO_x(MoS_2)$/Ni-g-C_3N_4 step-scheme heterojunctions with enhanced photo- and electro-catalytic performance, *J. Power Sources*, 2021, **510**, 230420.
9 Z. Wang, J. Bao, W. Liu, L. Xu, Y. Hu, M. Guan, M. Zhou and H. Li, Strong electronic coupled $FeNi_3/Fe_2(MoO_4)_3$ nanohybrids for enhancing the electrocatalytic activity for the oxygen evolution reaction, *Inorg. Chem. Front.*, 2020, **7**, 2791–2798.
10 C. Zhang, Y. Xue, L. Hui, Y. Fang, Y. Liu and Y. Li, Graphdiyne@$NiO_x(OH)_y$ heterostructure for efficient overall water splitting, *Mater. Chem. Front.*, 2021, **5**, 5305–5311.
11 X. Y. Yu and X. W. Lou, Mixed Metal Sulfides for Electrochemical Energy Storage and Conversion, *Adv. Energy Mater.*, 2018, **8**, 1701592.
12 P. Yan, Q. Liu, H. Zhang, L. Qiu, H. B. Wu and X. Y. Yu, Deeply reconstructed hierarchical and defective NiOOH/FeOOH nanoboxes with accelerated kinetics for the oxygen evolution reaction, *J. Mater. Chem. A*, 2021, **9**, 15586–15594.
13 E. L. Hu, Y. F. Feng, J. W. Nai, D. Zhao, Y. Hu and X. W. Lou, Construction of hierarchical Ni-Co-P hollow nanobricks with oriented nanosheets for efficient overall water splitting, *Energy Environ. Sci.*, 2018, **11**, 872–880.
14 S. Geng, Y. Liu, Y. S. Yu, W. Yang and H. Li, Engineering defects and adjusting electronic structure on S doped MoO_2 nanosheets toward highly active hydrogen evolution reaction, *Nano Res.*, 2020, **13**, 121–126.
15 M. Zheng, K. Guo, W. J. Jiang, T. Tang, X. Wang, P. Zhou, J. Du, Y. Zhao, C. Xu and J. S. Hu, When MoS_2 meets FeOOH: A "one-stone-two-birds" heterostructure as a bifunctional electrocatalyst for efficient alkaline water splitting, *Appl. Catal., B*, 2019, **244**, 1004–1012.
16 W. Zhang, Y. Tang, L. Yu and X. Y. Yu, Activating the alkaline hydrogen evolution performance of Mo-incorporated $Ni(OH)_2$ by plasma-induced heterostructure, *Appl. Catal., B*, 2020, **266**, 118154.
17 Y. Zhai, X. Ren, J. Yan and S. Liu, High Density and Unit Activity Integrated in Amorphous Catalysts for Electrochemical Water Splitting, *Small Struct.*, 2021, **2**, 202000096.
18 L. Zhang, H. Zhao, S. Xu, Q. Liu, T. Li, Y. Luo, S. Gao, X. Shi, A. M. Asiri and X. Sun, Recent Advances in 1D Electrospun Nanocatalysts for Electrochemical Water Splitting, *Small Struct.*, 2021, **2**, 2000048.
19 B. Dong, J. Y. Xie, N. Wang, W. K. Gao, Y. Ma, T. S. Chen, X. T. Yan, Q. Z. Li, Y. L. Zhou and Y. M. Chai, Zinc ion induced three-dimensional Co_9S_8 nano-neuron network for efficient hydrogen evolution, *Renewable Energy*, 2020, **157**, 415–423.
20 Z. Yan, H. Sun, X. Chen, H. Liu, Y. Zhao, H. Li, W. Xie, F. Cheng and J. Chen, Anion insertion enhanced electrodeposition of robust metal hydroxide/oxide electrodes for oxygen evolution, *Nat. Commun.*, 2018, **9**, 2373.
21 Z. L. Zhao, Q. Wang, X. Huang, Q. Feng, S. Gu, Z. Zhang, H. Xu, L. Zeng, M. Gu and H. Li, Boosting Oxygen Evolution Reaction Using Defect-rich Ultra-Thin Ruthenium Oxide Nanosheets in Acidic Media, *Energy Environ. Sci.*, 2020, **13**, 5143–5151.
22 M. Xiao, L. Zhang, B. Luo, M. Lyu, Z. L. Wang, H. M. Huang, S. C. Wang, A. J. Du and L. Z. Wang, Molten-Salt-Mediated Synthesis of an Atomic Nickel Co-catalyst on TiO_2 for Improved Photocatalytic H_2 Evolution, *Angew. Chem., Int. Ed.*, 2020, **59**, 7230–7234.
23 H. Y. Jin, Q. F. Gu, B. Chen, C. Tang, Y. Zheng, H. Zhang, M. Jaroniec and S. Z. Qiao, Molten Salt-Directed Catalytic Synthesis of 2D Layered Transition-Metal Nitrides for Efficient Hydrogen Evolution, *Chem*, 2020, **6**, 2382–2394.
24 W. W. Han, L. L. Chen, B. Ma, J. Wang, W. Y. Song, X. B. Fan, Y. Li, F. B. Zhang and W. C. Peng, Ultra-small Mo_2C nanodots encapsulated in nitrogen-doped porous carbon for pH-universal hydrogen evolution: insights into the synergistic enhancement of HER activity by nitrogen doping and structural defects, *J. Mater. Chem. A*, 2019, **7**, 4734–4743.
25 C. H. Zhang and L. M. Dai, Targeted Defect Synthesis for Improved Electrocatalytic Performance, *Chem*, 2020, **6**, 1849–1851.
26 G. Qian, G. Yu, J. Lu, L. Luo, T. Wang, C. Zhang, R. Ku, S. Yin, W. Chen and S. Mu, Ultra-thin N-doped-graphene encapsulated Ni nanoparticles coupled with MoO_2 nanosheets for highly efficient water splitting at large current density, *J. Mater. Chem. A*, 2020, **8**, 14545–14554.
27 Z. H. Dong, F. Lin, Y. H. Yao and L. F. Jiao, Crystalline Ni $(OH)_2$/Amorphous $NiMoO_x$Mixed-Catalyst with Pt-Like Performance for Hydrogen Production, *Adv. Energy Mater.*, 2019, **9**, 1902703.
28 F. Q. He, X. H. Deng and M. Chen, Mechanism and kinetics of Fe(II) EDTA-NO reduction by iron powder under anaerobic condition, *Fuel*, 2016, **186**, 605–612.
29 H. Wang, H. Yuan, S. S. Hong, Y. Li and Y. Cui, Physical and chemical tuning of two-dimensional transition metal dichalcogenides, *Chem. Soc. Rev.*, 2015, **44**, 2664–2680.
30 D. Voiry, A. Mohite and M. Chhowalla, Phase engineering of transition metal dichalcogenides, *Chem. Soc. Rev.*, 2015, **44**, 2702–2712.
31 Z. M. Hu, X. Xiao, H. Y. Jin, T. Q. Li, M. Chen, Z. Liang, Z. F. Guo, J. Li, J. Wan, L. Huang, Y. R. Zhang, G. Feng and J. Zhou, Rapid mass production of two-dimensional metal oxides and hydroxides via the molten salts method, *Nat. Commun.*, 2017, **8**, 15630.
32 H. Sun, Z. Yan, F. Liu, W. Xu, F. Cheng and J. Chen, Self-Supported Transition-Metal-Based Electrocatalysts for

Hydrogen and Oxygen Evolution, *Adv. Mater.*, 2020, **32**, 1806326.

33 C. G. Kuai, Y. Zhang, L. L. Han, H. L. Xin, C. J. Sun, D. Nordlund, S. Z. Qiao, X. W. Du and F. Lin, Creating compressive stress at the NiOOH/NiO interface for water oxidation, *J. Mater. Chem. A*, 2020, **8**, 10747–10754.

34 X. Zhang, P. Yang and S. P. Jiang, Ni diffusion in vertical growth of MoS_2 nanosheets on carbon nanotubes towards highly efficient hydrogen evolution, *Carbon*, 2021, **175**, 176–186.

35 X. Zhao, J. Meng, Z. Yan, F. Cheng and J. Cheng, Nanostructured $NiMoO_4$ as active electrocatalyst for oxygen evolution, *Chin. Chem. Lett.*, 2019, **30**, 319–323.

36 K. Guo, Y. Wang, J. Huang, M. Lu, H. Li, Y. Peng, P. Xi, H. Zhang, J. Huang, S. Lu and C. Xu, In Situ Activated $Co_{3-x}Ni_xO_4$ as a Highly Active and Ultrastable Electrocatalyst for Hydrogen Generation, *ACS Catal.*, 2021, **11**, 8174–8182.

37 G. J. Liu, H. P. Bai, Y. J. Ji, L. Wang, Y. Z. Wen, H. P. Lin, L. R. Zheng, Y. Y. Li, B. Zhang and H. S. Peng, A highly efficient alkaline HER Co-Mo bimetallic carbide catalyst with an optimized Mo *d*-orbital electronic state, *J. Mater. Chem. A*, 2019, **7**, 12434–12439.

38 B. R. Garrett, S. M. Polen, M. Pimplikar, C. M. Hadad and Y. Wu, Anion-Redox Mechanism of $MoO(S_2)_2$(2,2′-bipyridine) for Electrocatalytic Hydrogen Production, *J. Am. Chem. Soc.*, 2017, **139**, 4342–4345.

39 W. B. Hu, Y. Liu, R. L. Withers, T. J. Frankcombe, L. Norén, A. Snashall, M. Kitchin, P. Smith, B. Gong, H. Chen, J. Schiemer, F. Brink and J. Wong-Leung, Electron-pinned defect-dipoles for high-performance colossal permittivity materials, *Nat. Mater.*, 2013, **12**, 821–826.

40 X. Chen, L. Liu, P. Y. Yu and S. S. Mao, Increasing solar absorption for photocatalysis with black hydrogenated titanium dioxide nanocrystal, *Science*, 2011, **331**, 746–750.

41 S. H. Jiang, R. Y. Zhang, H. X. Liu, Y. Rao, Y. N. Yu, S. Chen, Q. Yue, Y. N. Zhang and Y. J. Kang, Promoting Formation of Oxygen Vacancies in Two-Dimensional Cobalt-Doped Ceria Nanosheets for Efficient Hydrogen Evolution, *J. Am. Chem. Soc.*, 2020, **142**, 6461–6466.

42 T. Shinagawa, A. T. Garcia-Esparza and K. Takanabe, Insight on Tafel slopes from a microkinetic analysis of aqueous electrocatalysis for energy conversion, *Sci. Rep.*, 2015, **5**, 13801.

43 K. Xu, H. Ding, M. X. Zhang, M. Chen, Z. K. Hao, L. D. Zhang, C. Z. Wu and Y. Xie, Regulating Water-Reduction Kinetics in Cobalt Phosphide for Enhancing HER Catalytic Activity in Alkaline Solution, *Adv. Mater.*, 2017, **29**, 1606980.

44 J. B. Goodenough, Metallic oxides, *Prog. Solid State Chem.*, 1971, **5**, 145–399.

45 X. Liu, K. Chen, X. Y. Li, Q. C. Xu, J. Weng and J. Xu, Electron Matters: Recent Advances in Passivation and Applications of Black Phosphorus, *Adv. Mater.*, 2021, **33**, 202005924.

46 C. Wei, Y. M. Sun, G. G. Scherer, A. C. Fisher, M. Sherburne, J. W. Ager and Z. C. Xu, Surface Composition Dependent Ligand Effect in Tuning the Activity of Nickel-Copper Bimetallic Electrocatalysts toward Hydrogen Evolution in Alkaline, *J. Am. Chem. Soc.*, 2020, **142**, 7765–7775.

